

# The observational signature of the first H II regions

Thomas H. Greif<sup>1,4\*</sup>, Jarrett L. Johnson<sup>2,3</sup>, Ralf S. Klessen<sup>1</sup> and Volker Bromm<sup>2,3</sup>

<sup>1</sup> *Zentrum für Astronomie der Universität Heidelberg, Institut für Theoretische Astrophysik, Albert-Ueberle-Straße 2, 69120 Heidelberg, Germany*

<sup>2</sup> *Department of Astronomy, University of Texas, Austin, TX 78712, USA*

<sup>3</sup> *Texas Cosmology Center, University of Texas, Austin, TX 78712, USA*

<sup>4</sup> *Fellow of the International Max Planck Research School for Astronomy and Cosmic Physics at the University of Heidelberg*

29 June 2018

## ABSTRACT

We use three-dimensional smoothed particle hydrodynamics simulations together with a dynamical ray-tracing scheme to investigate the build-up of the first H II regions around massive Population III stars in minihaloes. We trace the highly anisotropic breakout of the ionising radiation into the intergalactic medium, allowing us to predict the resulting recombination radiation with greatly increased realism. Our simulations, together with Press-Schechter type arguments, allow us to predict the Population III contribution to the radio background at  $\sim 100$  MHz via bremsstrahlung and 21 cm emission. We find a global bremsstrahlung signal of around 1 mK, and a combined 21 cm signature which is an order of magnitude larger. Both might be within reach of the planned Square Kilometer Array experiment, although detection of the free-free emission is only marginal. The imprint of the first stars on the cosmic radio background might provide us with one of the few diagnostics to test the otherwise elusive minihalo star formation site.

**Key words:** cosmology: observations – cosmology: theory – early Universe – stars: formation

## 1 INTRODUCTION

One of the most important questions in modern cosmology is to understand how the first stars, the so-called Population III (Pop III), ended the cosmic dark ages at redshifts  $z \lesssim 30$  (Barkana & Loeb 2001; Bromm & Larson 2004; Ciardi & Ferrara 2005). Their emergence led to a fundamental transformation in the early Universe, from its simple initial state to one of ever increasing complexity. The emission from the hot,  $T_{\text{eff}} \sim 10^5$  K, photospheres of Pop III stars began the reionisation of primordial hydrogen and helium in the intergalactic medium (IGM), although this process was completed only later on, when more massive galaxies formed (Fan et al. 2006). In addition, the supernova explosions that ended the lives of massive Pop III stars distributed the first heavy elements into the IGM (Bromm et al. 2003; Greif et al. 2007; Tornatore et al. 2007; Wise & Abel 2008). This latter process might have had a significant impact on the physics of early star formation, as metal-enriched gas can cool more efficiently than primordial gas (Bromm & Loeb 2003; Omukai et al. 2005; Jappsen et al. 2007, 2009).

Based on numerical simulations, a general consensus has emerged that the first stars formed in dark matter mini-

haloes at  $z \sim 20 - 30$ , in isolation or at most as a small stellar multiple, and with typical masses of  $M_* \sim 100 M_{\odot}$  (for a recent review, see Bromm et al. 2009). It is crucial to observationally test this key prediction. However, it has become evident that this will be very challenging. Even the exquisite near-IR ( $\sim$  nJy) sensitivity of the upcoming *James Webb Space Telescope (JWST)* will not suffice to directly image such massive, single Pop III stars (Bromm et al. 2001; Gardner et al. 2006), unless they explode as energetic pair-instability supernovae (Heger & Woosley 2002; Scannapieco et al. 2005). The direct spectroscopic detection of recombination line emission from the H II region surrounding the Pop III star, as well as from the relic H II region left behind once the star had died, is beyond the capability of *JWST* as well, although such line emission might be detectable from primordial stellar populations inside more massive host haloes (Schaerer 2002, 2003; Johnson et al. 2009).

An alternative approach is to search for the global signature from many Pop III stars that formed in minihaloes over large cosmic volumes (Haiman & Loeb 1997). One such probe is the optical depth to Thomson scattering of cosmic microwave background (CMB) photons off free electrons along the line of sight, determined by the five-year *Wilkinson Microwave Anisotropy Probe (WMAP)* measurement to be  $\tau_e \simeq 0.09 \pm 0.02$  (Komatsu et al. 2009). This

\* E-mail: tgreif@ita.uni-heidelberg.de

signal, however, is dominated by ionising sources that must have formed closer to the end of reionisation, with only a small contribution from Pop III stars formed in minihaloes (Greif & Bromm 2006; Schleicher et al. 2008). A second empirical signature is the combined bremsstrahlung emission from the H II regions in their active and relic states around those minihaloes that hosted Pop III stars. The resulting free-free radio emission leads to spectral distortions that might be detectable in the Rayleigh-Jeans part of the CMB spectrum. Recently, the ARCADE 2 experiment has attempted to measure such a free-free contribution from the epoch of the first stars (Kogut et al. 2006). The surprisingly strong signal found, however, cannot originate in early Pop III stars, and in any case would overwhelm the much weaker contribution from the first stars and galaxies (Seiffert et al. 2009). The most promising detection strategy might be to scrutinise the background from the redshifted 21 cm line of neutral hydrogen (Furlanetto et al. 2006). Once the central Pop III star has died, the relic H II region left behind would provide a bright source of 21 cm emission (Tokutani et al. 2009). Again, individual sources are much too weak to leave a detectable imprint, but the planned Square Kilometer Array (SKA) might be able to detect the cumulative signal (Furlanetto 2006; Lazio 2008).

We here carry out radiation hydrodynamics simulations of the evolution of H II regions around massive Pop III stars in minihaloes, giving us a detailed understanding of the properties of individual sources. We combine this with an approximate, Press-Schechter type analysis of the cosmological number density of minihaloes as a function of redshift to derive the observational signature of the first H II regions as well as relic H II regions, where we specifically focus on the free-free and 21 cm probes. We note that we do not include the feedback effects exerted by black holes or supernovae, which are possible end products of massive Pop III stars (Heger & Woosley 2002). In this sense, we organise our work as follows. In Section 2, we describe the simulation setup and our implementation of the radiative transfer scheme in the smoothed particle hydrodynamics (SPH) code GADGET-2 (Springel 2005). In Section 3, we discuss the properties of the first H II regions in their active as well as relic states and their observational signature in terms of recombination radiation, bremsstrahlung and 21 cm emission. Finally, in Section 4 we summarise our results and assess their implications. For consistency, all quoted distances are physical, unless noted otherwise.

## 2 NUMERICAL METHODOLOGY

Our treatment of ionising and photodissociating radiation emitted by massive Pop III stars is very similar to the methodology introduced in Johnson et al. (2007) and Yoshida et al. (2007), with the exception that we here take the hydrodynamical response into account, self-consistently coupled to the chemical and thermal evolution of the gas. This allows us to model dense (D-type) as well as rarefied (R-type) ionisation fronts, which is crucial for a proper treatment of the breakout of ionising radiation. In the following, we describe our simulation setup, as well as the numerical implementation of the ray-tracing algorithm.

### 2.1 Simulation set-up

We perform our simulations in a cosmological box with linear size 200 kpc (comoving), and  $256^3$  particles per species, corresponding to a particle mass of  $\simeq 17 M_\odot$  for dark matter and  $\simeq 3 M_\odot$  for gas. The simulations are initialised at  $z = 99$  with a fluctuation power spectrum determined by a  $\Lambda$  cold dark matter ( $\Lambda$ CDM) cosmology with matter density  $\Omega_m = 1 - \Omega_\Lambda = 0.27$ , baryon density  $\Omega_b = 0.046$ , Hubble parameter  $h = H_0/100 \text{ km s}^{-1} \text{ Mpc}^{-1} = 0.7$ , where  $H_0$  is the Hubble expansion rate today, and spectral index  $n_s = 0.96$  (Komatsu et al. 2009). We use an artificially high fluctuation power of  $\sigma_8 = 1.6$  to accelerate structure formation in our relatively small box, although the cosmological mean is given by  $\sigma_8 = 0.81$ . We take the chemical evolution of the gas into account by following the abundances of H,  $\text{H}^+$ ,  $\text{H}^-$ ,  $\text{H}_2$ ,  $\text{H}_2^+$ , He,  $\text{He}^+$ ,  $\text{He}^{++}$ , and  $e^-$ , as well as the three deuterium species D,  $\text{D}^+$ , and HD. We include all relevant cooling mechanisms, i.e. H and He collisional ionisation, excitation and recombination cooling, bremsstrahlung, inverse Compton cooling, and collisional excitation cooling via  $\text{H}_2$  and HD (Glover & Jappsen 2007). We explicitly include  $\text{H}_2$  cooling via collisions with protons and electrons, which is important for the chemical and thermal evolution of relic H II region gas (Glover & Abel 2008).

We run the simulations until the first minihalo in the box has collapsed to a density of  $n_{\text{H}} = 10^4 \text{ cm}^{-3}$ , at which point the gas has cooled to  $\simeq 200 \text{ K}$  and becomes Jeans-unstable (Abel et al. 2002; Bromm et al. 2002). The first halo that fulfils this criterion collapses at  $z_* \simeq 20$  and has a virial mass of  $\simeq 9.4 \times 10^5 M_\odot$  and a virial radius of  $\simeq 90 \text{ pc}$ . Highly resolved simulations have shown that at later times, the gas condenses further under the influence of self-gravity to  $n_{\text{H}} \sim 10^{21} \text{ cm}^{-3}$ , where it becomes optically thick and forms a protostellar seed (Yoshida et al. 2008). Due to its residual angular momentum, the central clump flattens and likely evolves into an accretion disk. In our case, we find a flattened structure already at a density of  $n_{\text{H}} = 10^4 \text{ cm}^{-3}$  (see Fig. 1). Subsequently, the star grows to as massive as  $\sim 100 M_\odot$  within its lifetime of a few million years (Bromm & Loeb 2004). However, we note that under certain conditions the disk may fragment to form multiple objects of smaller masses (Clark et al. 2008). Unfortunately, the details of the accretion phase and the concomitant radiative feedback are poorly understood, although some analytic investigations have been carried out (Tan & McKee 2004; McKee & Tan 2008). Under these circumstances, it seems best to initialise the calculation of the H II region at the onset of the initial Jeans-instability, when the density exceeds  $n_{\text{H}} = 10^4 \text{ cm}^{-3}$ .

### 2.2 Ray-tracing scheme

The procedure used to calculate the Strömgren sphere around the star for a given time-step  $\Delta t$  is similar to the ray-tracing scheme used in Johnson et al. (2007). We first designate an individual SPH particle as the source of ionising radiation and create a spherical grid with typically  $10^5$  rays and 500 logarithmically spaced radial bins around the source particle. The minimum radius is set by the smoothing length of the central particle, while the maximum radius is chosen appropriately to encompass the entire H II region. This ap-

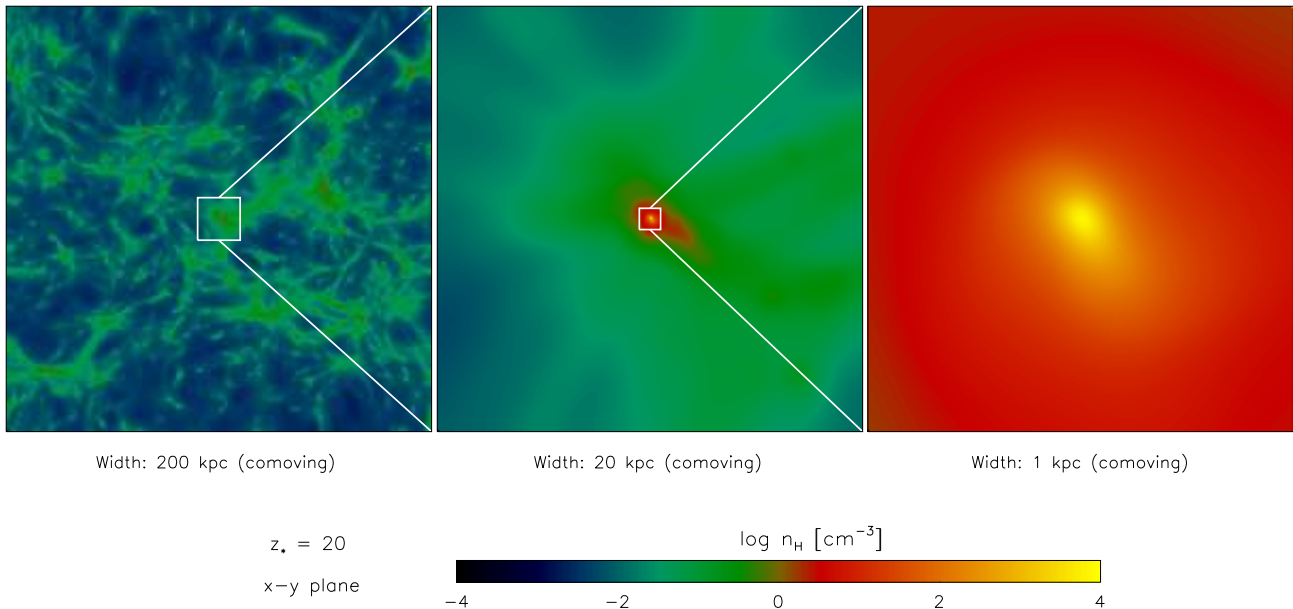


**Figure 1.** Sequential zoom-in on the first star-forming minihalo at  $z_* \simeq 20$ . Shown is the density-squared weighted average of the hydrogen density along the line of sight, just after the formation of the first Jeans-unstable clump in a  $\simeq 9.4 \times 10^5 M_\odot$  minihalo. The flattening of the core due to angular momentum conservation during the collapse is marginally visible, with the consequence that ionising radiation from the central source breaks out anisotropically (see Fig. 3).

proach may seem crude compared to existing methods that use adaptive grids (e.g. HEALPix; Górski et al. 2005), but the increased angular and radial resolution towards the center tend to mirror the existing density profile. However, one must proceed with care if the ionisation front encounters dense clumps far from the source, where the resolution may no longer be sufficient.

In a single, parallel loop, the Cartesian coordinates of all particles are converted to spherical coordinates, such that their density and chemical abundances are mapped to the bins corresponding to their radius, zenith angle and azimuth, denoted by  $r$ ,  $\theta$  and  $\phi$ , respectively. The volume of each particle is approximately given by  $\Delta V \simeq h^3$ , which transforms to  $\Delta r = h$ ,  $\Delta \theta = h/r$  and  $\Delta \phi = h/(r \sin \theta)$ . If the volume element of a particle intersects with the volume element of a bin, the particle contributes to the bin proportional to the density of the particle squared. This dependency ensures that overdense regions are not missed if the bin size is much larger than the smoothing length, which could occur far from the source where the grid resolution is poor. Accidental flash-ionisation of minihaloes is thus avoided. Once the above steps are complete, it is straightforward to solve the ionisation front equation along each ray:

$$n_n r_I^2 \frac{dr_I}{dt} = \frac{\dot{N}_{\text{ion}}}{4\pi} - \alpha_B \int_0^{r_I} n_e n_+ r^2 dr, \quad (1)$$

where  $r_I$  denotes the position of the ionisation front,  $\dot{N}_{\text{ion}}$  the number of ionising photons emitted per second,  $\alpha_B$  the case B recombination coefficient, and  $n_n$ ,  $n_e$  and  $n_+$  the number densities of neutral particles, electrons and positively charged ions, respectively. We assume that the recombination coefficient remains constant at its value for  $10^4$  K, which is roughly the temperature of the H II and He III region.

The numbers of H I/He I and He II ionising photons are given by

$$\dot{N}_{\text{ion}} = \frac{\pi L_*}{\sigma T_{\text{eff}}^4} \int_{\nu_{\text{min}}}^{\infty} \frac{B_\nu}{h\nu} d\nu, \quad (2)$$

where  $h$  from now on denotes Planck's constant,  $\sigma$  denotes Boltzmann's constant, and  $\nu_{\text{min}}$  is the minimum frequency corresponding to the ionisation threshold of H I and He II. We assume that massive Pop III stars emit a blackbody spectrum  $B_\nu$  (in  $\text{erg s}^{-1} \text{cm}^{-2} \text{Hz}^{-1} \text{sr}^{-1}$ ) with an effective temperature  $T_{\text{eff}} = \text{dex}(4.922, 4.975, 4.999)$  K and luminosity  $L_* = \text{dex}(5.568, 6.095, 6.574)$   $L_\odot$  for a 50, 100 and 200  $M_\odot$  star, respectively (Schaerer 2002). This yields

$$\dot{N}_{\text{ion,H I/He I}} = [2.80, 9.14, 26.99] \times 10^{49} \text{ s}^{-1} \quad (3)$$

and

$$\dot{N}_{\text{ion,He II}} = [0.72, 4.14, 15.43] \times 10^{48} \text{ s}^{-1}. \quad (4)$$

We do not distinguish between the H II and He II region, which is a good approximation for massive Pop III stars (Osterbrock & Ferland 2006). The lifetimes of the stars are given by  $t_* = 3.7, 2.7$  and  $2.2$  Myr, respectively. We neglect the effects of stellar evolution, which might lead to a decrease of the number of ionising photons emitted at the end of the main sequence (Marigo et al. 2001; Schaerer 2002), although recent investigations have shown that rotating Pop III stars remain on bluer evolutionary tracks and this effect might not be so strong (Yoon & Langer 2005; Woosley & Heger 2006; Vázquez et al. 2007).

To obtain a discretisation of the ionisation front equation, we replace the integral on the right-hand side of equation (1) by a discrete sum:

$$\int_0^{r_I} n_e n_+ r^2 dr \simeq \sum_i n_{e,i} n_{+,i} r_i^2 \Delta r_i, \quad (5)$$

where  $\Delta r_i$  is the radial extent of bin  $i$ , and the sum extends from the origin to the position of the ionisation front at

the end of the current time-step  $\Delta t$ . The above equation describes the advancement of the ionisation front due to an excess of ionising photons compared to recombinations. Similarly, the left-hand side of equation (1), which models the propagation of the ionisation front into neutral gas, is discretised by

$$n_n r_I^2 \frac{dr_I}{dt} \simeq \frac{1}{\Delta t} \sum_i n_{n,i} r_i^2 \Delta r_i, \quad (6)$$

where the sum now extends from the position of the ionisation front at the previous time-step to its position at the end of the current time-step. We perform the above steps separately for the H II and He III region, since they require distinct heating and ionisation rates. For the He III region, we replace the quantities  $n_n$  and  $n_+$  in equation (1) with  $n_n = f_{\text{HeII}} n_{\text{H}}$  and  $n_+ = f_{\text{HeIII}} n_{\text{H}}$ , where  $f_X$  is the number density of species  $X$  relative to  $n_{\text{H}}$ . We adopt a case B recombination rate of  $\alpha_{\text{B}} = 1.3 \times 10^{-12} \text{ cm}^3 \text{ s}^{-1}$  for He III recombinations to He II (Osterbrock & Ferland 2006). Applying the same prescription to the H II region, we find  $n_n = (f_{\text{HI}} + f_{\text{HeI}}) n_{\text{H}}$  and  $n_+ = (f_{\text{HII}} + f_{\text{HeII}}) n_{\text{H}}$ . Similarly, we adopt a case B recombination rate of  $\alpha_{\text{B}} = 2.6 \times 10^{-13} \text{ cm}^3 \text{ s}^{-1}$  for hydrogen and helium recombinations from their first ionised states to the ground state (Osterbrock & Ferland 2006). We initialise the calculation of the H II region at the boundary of the He III region, since hydrogen and helium are maintained in their first ionisation states by recombinations of He III to He II (Osterbrock & Ferland 2006). We note that the exact position of the ionisation front is not restricted to integer multiples of our pre-defined radial bins, but may instead lie anywhere in between. For this purpose we adopt a simple linear scaling of the number of ionisations and recombinations as a function of the relative position of the ionisation front. The most expensive step in terms of computing time is the assignment of the density and the chemical abundances to the grid, while the ray-tracing itself requires only a negligible amount of time.

### 2.3 Photoionisation and photoheating

Once the extent of the H II and He III region have been determined, the SPH particles within these regions are assigned an additional variable that stores their distance from the source. This information is then passed to the chemistry solver, which determines the ionisation and heating rates, given by

$$k_{\text{ion}} = \int_{\nu_{\text{min}}}^{\infty} \frac{F_{\nu} \sigma_{\nu}}{h\nu} d\nu \quad (7)$$

and

$$\Gamma = n_n \int_{\nu_{\text{min}}}^{\infty} F_{\nu} \sigma_{\nu} \left(1 - \frac{\nu_{\text{min}}}{\nu}\right) d\nu, \quad (8)$$

where  $F_{\nu}$  and  $\sigma_{\nu}$  denote the incoming specific flux and ionisation cross section, respectively. For the case of a blackbody,

$$F_{\nu} = \frac{L_*}{4\sigma T_{\text{eff}}^4 r^2} B_{\nu}, \quad (9)$$

where  $r$  is the distance from the source. The resulting rates are given by

$$k_{\text{ion,HI}} = \frac{[0.45, 1.32, 3.69] \times 10^{-6}}{(r/\text{pc})^2} \text{ s}^{-1}, \quad (10)$$

$$k_{\text{ion,HeI}} = \frac{[0.42, 1.43, 4.29] \times 10^{-6}}{(r/\text{pc})^2} \text{ s}^{-1}, \quad (11)$$

$$k_{\text{ion,HeII}} = \frac{[0.67, 3.72, 13.57] \times 10^{-8}}{(r/\text{pc})^2} \text{ s}^{-1}, \quad (12)$$

$$\Gamma_{\text{HI}} = n_{\text{HI}} \frac{[0.40, 1.28, 3.74] \times 10^{-17}}{(r/\text{pc})^2} \text{ erg s}^{-1} \text{ cm}^{-3}, \quad (13)$$

$$\Gamma_{\text{HeI}} = n_{\text{HeI}} \frac{[0.41, 1.57, 4.94] \times 10^{-17}}{(r/\text{pc})^2} \text{ erg s}^{-1} \text{ cm}^{-3}, \quad (14)$$

$$\Gamma_{\text{HeII}} = n_{\text{HeII}} \frac{[0.72, 4.46, 17.13] \times 10^{-19}}{(r/\text{pc})^2} \text{ erg s}^{-1} \text{ cm}^{-3} \quad (15)$$

for a 50, 100 and 200  $M_{\odot}$  Pop III star, respectively. These are taken into account every time-step, while the ray-tracing is performed only every fifth time-step. Since the hydrodynamic time-step is generally limited to one twentieth of the sound-crossing time through the kernel, our treatment of the coupled evolution of the ionisation front and the hydrodynamic shock is roughly correct. The computational cost of runs with and without ray-tracing are typically within a factor of a few.

### 2.4 Photodissociation and photodetachment

The final ingredient in our algorithm is the inclusion of molecule-dissociating radiation. This effect turns out to be of only minor importance in the present study, but will render our algorithm capable of addressing a general set of early Universe applications. Molecular hydrogen is the most important coolant in low-temperature, primordial gas, but is easily destroyed by radiation in the Lyman-Werner (LW) bands between 11.2 and 13.6 eV. The small residual  $\text{H}_2$  fraction in the IGM leads to a very small optical depth over cosmological distances, such that even a small background can have a significant effect (Haiman et al. 2000; Glover & Brand 2001; Johnson et al. 2007). In our implementation, we do not take self-shielding into account, which becomes important for  $\text{H}_2$  column densities  $\gtrsim 10^{14} \text{ cm}^{-2}$  (Draine & Bertoldi 1996). Such a high column density is difficult to achieve in minihaloes, and is more likely to occur within the virial radius of the first galaxies (Oh & Haiman 2002). However, the onset of turbulence in the first galaxies likely leads to a reduction of self-shielding via Doppler shifting (Wise & Abel 2007; Greif et al. 2008). For this reason we treat the photodissociation of  $\text{H}_2$  in the optically thin limit, such that the dissociation rate in a volume limited by causality to a radius  $r = ct_*$  is given by  $k_{\text{H}_2} = 1.1 \times 10^8 F_{\text{LW}} \text{ s}^{-1}$ , where  $F_{\text{LW}}$  is the integral of the specific flux  $F_{\nu}$  over the LW bands, resulting in

$$k_{\text{H}_2} = \frac{[1.27, 3.38, 9.07] \times 10^{-7}}{(r/\text{pc})^2} \text{ s}^{-1} \quad (16)$$

for a 50, 100 and 200  $M_{\odot}$  Pop III star, respectively. We equate the photodissociation rate of hydrogen deuteride to that of molecular hydrogen. In the present work, we do not explicitly include photodetachment of  $\text{H}^-$  and photodissociation of  $\text{H}_2^+$ , which might be problematic outside of the H II region, where molecules survive collisional destruction.

However, in the context discussed here, this caveat is not important (see Johnson et al. 2007).

### 3 OBSERVATIONAL SIGNATURE

In the following, we discuss the direct observational signature of the first H II regions and relic H II regions in terms of recombination radiation, as well as their indirect signature in terms of a global radio background produced by bremsstrahlung and 21 cm emission.

#### 3.1 Build-up of H II and He III region

The build-up of the first H II regions by Pop III stars in minihaloes was treated in one dimension by Kitayama et al. (2004) and Whalen et al. (2004), and in three dimensions by Alvarez et al. (2006), Abel et al. (2007) and Yoshida et al. (2007). The latter also treated the build-up of a smaller He III region, which is created by the very hard spectrum of massive Pop III stars. The consensus was that recombinations initially balanced ionisations within the virial radius of the host halo, leading to the formation of a D-type ionisation front. Breakout occurred after the density dropped sufficiently for the ionisation front to race ahead of the hydrodynamic shock, becoming R-type. The hydrodynamic response of the gas is self-similar, since minihaloes approximately resemble singular isothermal spheres (Shu et al. 2002; Alvarez et al. 2006). The relevant parameters are set by the temperature of the singular isothermal sphere and the H II region, which in our case are  $T \simeq 200$  and  $\simeq 10^4$  K, respectively.

In Fig. 2, we compare the density profile of the Shu et al. (2002) solution to the simulation for the case of a  $100 M_{\odot}$  Pop III star. Interestingly, we find a clear deviation from the ideal, spherically symmetric solution already during the D-type phase, which is caused by the anisotropic collapse of the minihalo. Due to angular momentum conservation, the gas spins up and forms a flattened, disk-like structure at a density of  $10^4 \text{ cm}^{-3}$ , which can be seen in the right panel of Fig. 1, and in the left panel of Fig. 2, where it is evident that the density dispersion is almost an order of magnitude within the central  $\simeq 10$  pc. In response to this anisotropy, which is further amplified by the density-squared dependence of recombinations, the ionisation front first breaks out perpendicular to the disk, where the column density is lowest. This is visible in the left and middle panels of Fig. 3, as well as in Fig. 2, where the Shu et al. (2002) solution is approximately reproduced perpendicular to the disk, while the plane of the disk remains neutral and dense. Once the ionisation front becomes R-type, spherical symmetry is asymptotically restored and the H II region expands to  $r_{\text{HII}} \simeq 1.9, 2.7$  and  $3.7$  kpc for the  $50, 100$  and  $200 M_{\odot}$  Pop III star, respectively. We find that He II ionising photons within the He III region increase the central temperature by a factor of  $\simeq 1.5$ , leaving only a small imprint on the dynamical evolution of the H II region (see Yoshida et al. 2007). However, the He II  $\lambda 1640$  recombination line within the He III region may be used as a distinct probe for the presence of massive Pop III stars (Bromm et al. 2001; Oh 2001; Tumlinson et al. 2001; Schaerer 2002). In the following, we

use the results obtained in this section to determine the recombination signature of the first H II and He III regions in their active as well as relic states.

#### 3.2 Recombination radiation from individual H II and He III regions

The strongest direct signature of the first H II and He III regions is likely generated by recombination radiation, since ionizing photons are absorbed by dense gas in the host halo. We here concentrate on the  $\text{H}\alpha$  and He II  $\lambda 1640$  lines, since more energetic photons are scattered out of resonance by the neutral IGM, creating extended haloes around high-redshift sources (e.g. Loeb & Rybicki 1999). The resulting fluxes may then be compared to the expected sensitivity of the Mid-Infrared Instrument (MIRI) on *JWST* at  $\sim 10 \mu\text{m}$  wavelengths (Gardner et al. 2006). The spatial resolution is limited by diffraction, such that a scale of  $\simeq 1$  kpc at  $z = 20$  is marginally resolved, which allows us to approximate the region of emission as a point source. Using the simulation output, the total luminosities are given by

$$L_{\text{H}\alpha} = j_{\text{H}\alpha} \sum_i \frac{m_i}{\rho_i} \left( \frac{X\rho_i}{m_{\text{H}}} \right)^2 f_{e,i} f_{\text{HII},i} \quad (17)$$

and

$$L_{1640} = j_{1640} \sum_i \frac{m_i}{\rho_i} \left( \frac{X\rho_i}{m_{\text{H}}} \right)^2 f_{e,i} f_{\text{HeIII},i}, \quad (18)$$

where  $j_{\text{H}\alpha}$  and  $j_{1640}$  are the emissivity of the  $\text{H}\alpha$  and He II  $\lambda 1640$  lines at  $10^4$  K (Osterbrock & Ferland 2006),  $X = 0.76$  is the primordial mass fraction of hydrogen,  $m_{\text{H}}$  is the mass of the hydrogen atom,  $m_i$  and  $\rho_i$  are the mass and density of particle  $i$ , respectively, and the sum is over all particles in the simulation box. From the total luminosity, we determine the observed flux with the inverse-square law

$$F = \frac{L}{4\pi D_{\text{L}}^2}, \quad (19)$$

where  $D_{\text{L}}$  is the cosmological luminosity distance. In Fig. 4, we show the observed flux for a  $50, 100$  and  $200 M_{\odot}$  Pop III star as a function of time. The emission peaks before breakout, when the density in the host halo is still high, reaching a maximum flux of  $\simeq 10^{-23} \text{ erg s}^{-1} \text{ cm}^{-2}$ . Once the star turns off, the  $\text{H}\alpha$  emission drops quite rapidly over the course of a few 10 Myr, while the He II  $\lambda 1640$  emission drops almost instantaneously in the  $100$  and  $200 M_{\odot}$  cases, due to the high recombination coefficient of He III to He II. It is noteworthy that the emission in the He II  $\lambda 1640$  line is generally not much lower than that in the  $\text{H}\alpha$  line, which may be used as an indicator for massive Pop III stars (Bromm et al. 2001; Oh 2001; Tumlinson et al. 2001; Schaerer 2002).

For a  $10\sigma$  detection with an exposure time of 100 hours, the spectrograph on MIRI exhibits a typical limiting sensitivity of  $\simeq 10^{-18} \text{ erg s}^{-1} \text{ cm}^{-2}$  (Panagia 2005), implying that the first H II regions are typically five orders of magnitude too faint for a direct detection. We must therefore resort to indirect methods that rely on their cumulative signal. One such signature is the cosmic infrared background (CIB), where the redshifted Ly $\alpha$  recombination photons from  $z \sim 10 - 20$  might contribute at a detectable level (Santos et al. 2002; Kashlinsky et al. 2005). Minihaloes, however, are not

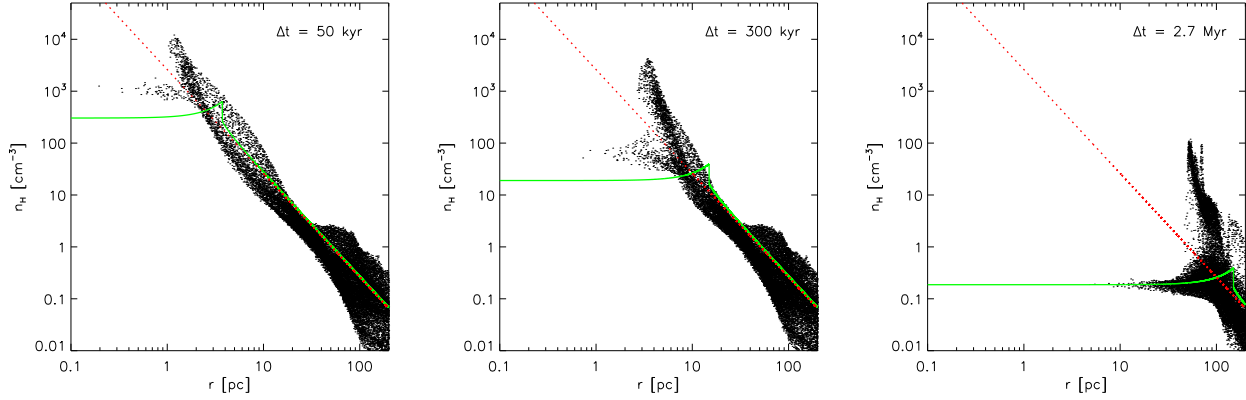


**Figure 2.** The hydrodynamic response of the gas to photoheating by a  $100 M_{\odot}$  Pop III star after 50 kyr, 300 kyr, and 2.7 Myr (from left to right). Shown is the hydrogen density as a function of radius for the simulation (black dots) and the analytic Shu et al. (2002) solution (green solid line), as well as the initial density profile of a singular isothermal sphere with 200 K (red dotted line). The functional form of the analytic solution is reproduced perpendicular to the disk, where the ionisation front breaks out after only a few 10 kyr. However, this is not the case in the plane of the disk, where the gas remains neutral and dense until the end of the star’s lifetime.

expected to be important sources for the CIB, as opposed to more massive dark matter haloes that host the first galaxies (Greif & Bromm 2006). This leads us to consider the radio background as a key diagnostic of the Pop III minihalo formation site.

### 3.3 Radio background produced by bremsstrahlung

The first H II regions in their active as well as relic states also emit bremsstrahlung via thermal motions of electrons in an ionised medium. In line with our conclusions of the previous section, the signature from an individual source is much too faint to be detected. However, the cumulative radio signal might be strong enough to be detected by the upcoming SKA. We will here further explore this possibility (for a review of earlier work, see Furlanetto et al. 2006).

Solving the cosmological radiative transfer equation, it is straightforward to derive a simple expression for the observed radio background  $J_{\nu}$  (in  $\text{erg s}^{-1} \text{cm}^{-2} \text{Hz}^{-1} \text{sr}^{-1}$ ):

$$J_{\nu} = \int_0^{t_{H,0}} \frac{j_{\nu}}{(1+z)^3} c dt, \quad (20)$$

where  $t_{H,0}$  is the present Hubble time and  $j_{\nu}$  is the specific emissivity of bremsstrahlung, given by

$$j_{\nu} = \epsilon_{\text{ff}} \langle n_e^2 \rangle (T/10^3 \text{ K})^{-1/2}, \quad (21)$$

where  $\epsilon_{\text{ff}} \simeq 10^{-39} \text{ erg s}^{-1} \text{cm}^3 \text{Hz}^{-1} \text{sr}^{-1}$ ,  $\langle n_e^2 \rangle$  is the volume-averaged electron density, and  $T$  is the temperature (Rybicki & Lightman 1979). We universally assume  $T = 10^3 \text{ K}$ , since the relic H II region cools quite rapidly to  $\sim 10^3 \text{ K}$  via inverse Compton losses and adiabatic expansion once the star has died (e.g. Greif et al. 2007; Yoshida et al. 2007). Furthermore, we assume  $j_{\nu} = 0$  at  $z < 6$ , since photoheating during reionisation evaporates minihaloes (Dijkstra et al. 2004). This leads to:

$$J_{\nu} = c \epsilon_{\text{ff}} \int_{\infty}^6 \frac{\langle n_e^2 \rangle}{(1+z)^3} \left| \frac{dt}{dz} \right| dz, \quad (22)$$

where we relate  $\langle n_e^2 \rangle$  to the number density of minihaloes according to:

$$\langle n_e^2 \rangle \simeq t_{\text{rec}} n_{\text{H,b}}^2 V_{\text{HII}} \left| \frac{dN_{\text{ps}}}{dz} \right| \left| \frac{dz}{dt} \right|. \quad (23)$$

Here,  $t_{\text{rec}} = (\alpha_{\text{B}} n_{\text{H,b}})^{-1}$  denotes the recombination time for hydrogen atoms,  $\alpha_{\text{B}}$  the case B recombination rate for  $T = 10^3 \text{ K}$ ,  $n_{\text{H,b}}$  the background density,  $N_{\text{ps}}$  the number of minihaloes per comoving volume,  $V_{\text{HII}} = N_{\text{ion}}/n_{\text{H,b},0}$  the comoving volume of an individual H II region in its active as well as relic state, which is independent of redshift, and  $N_{\text{ion}} = \dot{N}_{\text{ion}} t_*$  the total number of ionising photons emitted per Pop III star (see Section 2). In the above equation, we have implicitly assumed that (relic) H II regions survive for a recombination time, and that all ionising photons escape into the IGM, which is a good approximation for massive Pop III stars in minihaloes (Alvarez et al. 2006). We note that in the range of redshifts considered here, the recombination time is larger than the stellar lifetime and smaller than the age of the Universe. In principle, one must also account for the clustering of minihaloes (biasing), which reduces the net volume filling factor of H II regions (Mo & White 1996; Iliev et al. 2003; Gao et al. 2005; Reed et al. 2005; Greif & Bromm 2006). However, it is extremely difficult to determine the importance of this effect, since (i) the actual overlap depends on the relative separation of minihaloes, and (ii) previous ionisation allows a nearby H II region to become larger than usual. We therefore neglect biasing, but keep in mind that the actual signal may be somewhat lower.

In equation (23), the number density of minihaloes is given by

$$N_{\text{ps}}(z) = \int_{M_{\text{min}}}^{M_{\text{max}}} n_{\text{ps}}(z, M) dM, \quad (24)$$

where  $n_{\text{ps}}$  is the well-known Press-Schechter mass function (Press & Schechter 1974). The minimum mass required for efficient cooling within a Hubble time may be found in Yoshida et al. (2003) and Trenti & Stiavelli (2009):

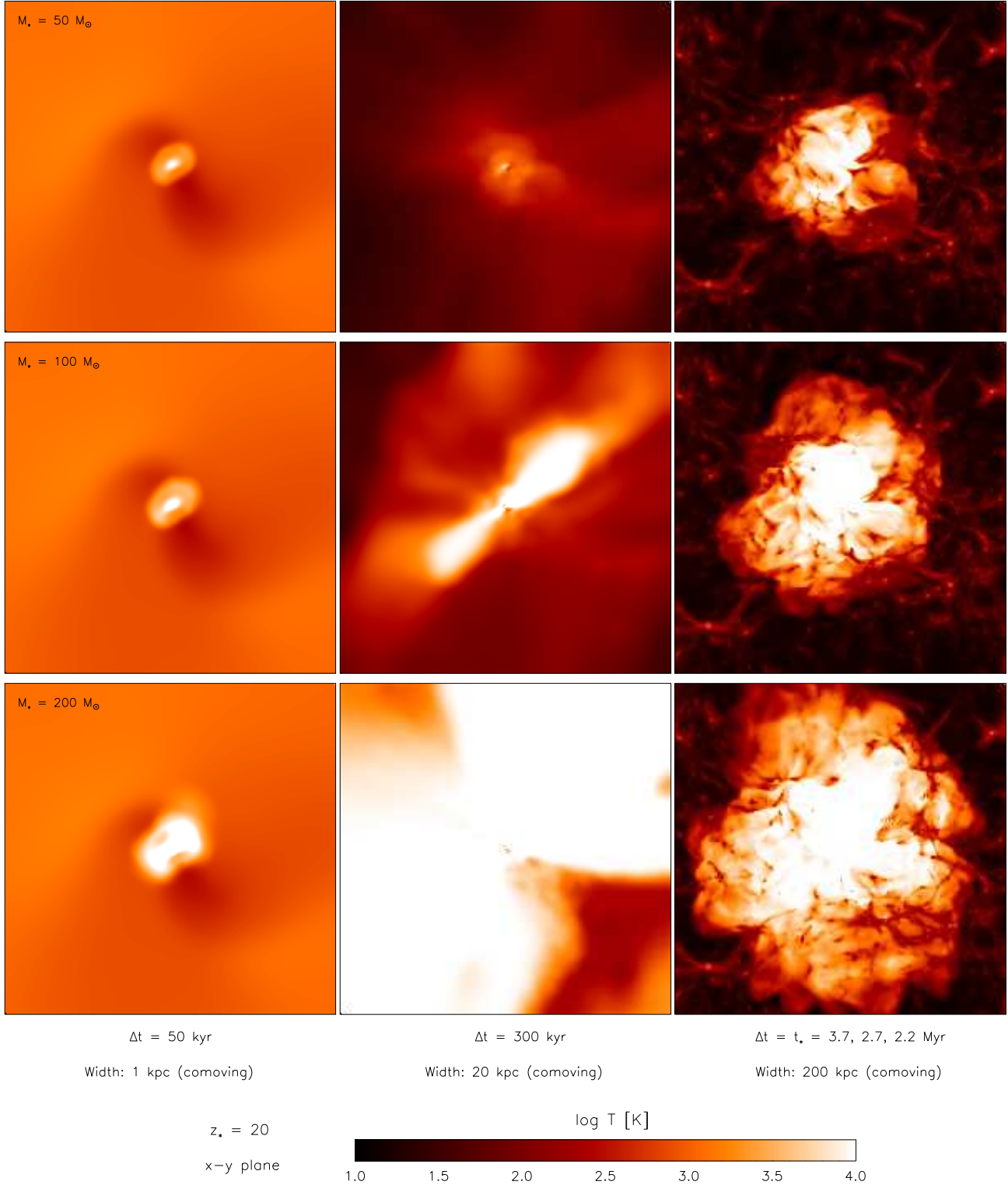


**Figure 3.** The H II region created by a 50, 100 and 200  $M_\odot$  Pop III star (from top to bottom) after 50 kyr, 300 kyr, and at the end of their lifetime (from left to right). Shown is the density-squared weighted average of the temperature along the line of sight. The spiral structure of the central clump as well as the resulting anisotropic breakout of the ionisation front are clearly visible. For increasing stellar mass and ionising photon output, breakout occurs earlier and is more isotropic. Once the ionisation front becomes R-type, spherical symmetry is asymptotically restored and the H II region expands to a final radius of  $r_{\text{HII}} \simeq 1.9, 2.7$  and 3.7 kpc after 3.7, 2.7 and 2.2 Myr, respectively.

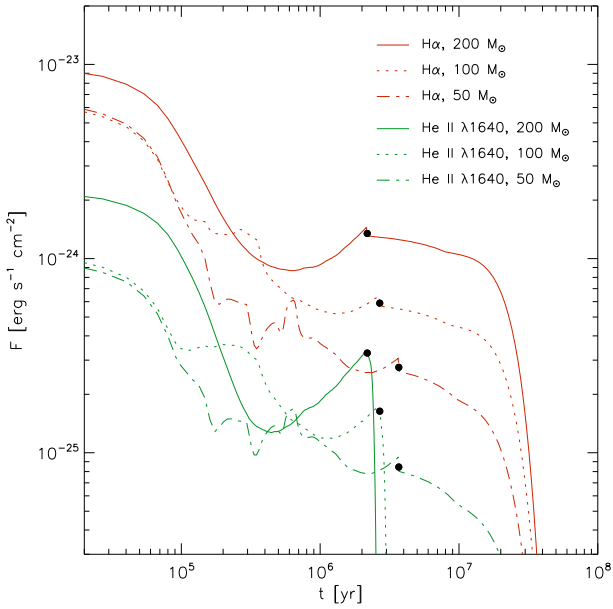


**Figure 4.** The observed recombination flux in H $\alpha$  and He II  $\lambda 1640$  for a 50, 100 and 200  $M_{\odot}$  Pop III star, shown as a function of time after reaching the zero-age main sequence (the black dots denote the end of their lifetimes). The emission peaks before breakout, when the density in the host halo is still high, reaching a maximum flux of  $\simeq 10^{-23}$  erg s $^{-1}$  cm $^{-2}$ . Once the star turns off, the H $\alpha$  emission drops quite rapidly over the course of a few 10 Myr, while the He II  $\lambda 1640$  emission drops almost instantaneously in the 100 and 200  $M_{\odot}$  cases, due to the high recombination coefficient of He III to He II. The emission in the He II  $\lambda 1640$  line is generally not much lower than that in the H $\alpha$  line, which is characteristic for a top-heavy IMF and may be used as an indicator for massive Pop III stars. For a  $10\sigma$  detection and an exposure time of 100 hours, the limiting sensitivity of the MIRI spectrograph on *JWST* is approximately  $10^{-18}$  erg s $^{-1}$  cm $^{-2}$ , indicating that the first H II regions are typically five orders of magnitude too faint to be detected directly.

$$M_{\min} \simeq 10^6 M_{\odot} \left( \frac{1+z}{10} \right)^{-2}, \quad (25)$$

while the maximum mass is set by the requirement that cooling must be dominated by molecular hydrogen, i.e. the virial temperature must not exceed  $T \simeq 10^4$  K for atomic hydrogen cooling, resulting in (e.g. Barkana & Loeb 2001)

$$M_{\max} \simeq 2.5 \times 10^7 M_{\odot} \left( \frac{1+z}{10} \right)^{-3/2}. \quad (26)$$

We have found that our results are only marginally affected by the upper mass limit, but depend sensitively on the lower mass limit, since most minihaloes reside at the lower end of the halo distribution function.

After combining the above equations, we obtain

$$J_{\nu} \simeq \frac{c \epsilon_{\text{ff}} N_{\text{ion}}}{\alpha_{\text{B}}} N_{\text{ps}} (z=6), \quad (27)$$

which, for an IMF consisting solely of 100  $M_{\odot}$  Pop III stars, yields

$$J_{\nu} \simeq 300 \text{ mJy sr}^{-1}. \quad (28)$$

The brightness temperature,  $T_b = c^2 J_{\nu} / 2k_{\text{B}} \nu^2$ , is given by

$$T_b \simeq 1 \text{ mK} \left( \frac{\nu}{100 \text{ MHz}} \right)^{-2}. \quad (29)$$

In the following, we investigate whether a signal of this magnitude is observable by the upcoming SKA.

The sensitivity of radio instruments is generally defined by the ratio of the effective collecting area  $A_e$  to the system temperature  $T_{\text{sys}}$ . For the SKA with its proposed aperture array configuration at low frequencies,  $A_e/T_{\text{sys}} \simeq 5 \times 10^3 \text{ m}^2 \text{ K}^{-1}$  at 100 MHz<sup>1</sup>. In this range, the system temperature is dominated by Galactic synchrotron emission, for which a useful approximation is given by  $T_{\text{sky}} \simeq 180 \text{ K} (\nu/180 \text{ MHz})^{-2.6}$  (Furlanetto et al. 2006), resulting in  $T_{\text{sys}} \simeq 800 \text{ K}$  and  $A_e \simeq 4 \times 10^6 \text{ m}^2$ . The minimum angular resolution for an array filling factor of unity at 100 MHz is approximately  $15'$ . At higher resolutions, the sensitivity decreases much too rapidly for effective imaging. In Fig. 5, we compare the sensitivity of the SKA for a  $10\sigma$  detection, a bandwidth of  $\Delta\nu_{\text{obs}} = 1 \text{ MHz}$ , and an integration time of 1000 h to the brightness temperature and specific flux expected for free-free emission. Although the figure implies that the free-free signal is detectable by the SKA, we have neglected biasing as well as radiative feedback in the form of a global LW background, which attenuates star formation in minihaloes (Johnson et al. 2007, 2008). Another complicating issue is the overlap with 21 cm emission, which makes it nearly impossible to isolate the contribution from bremsstrahlung. In consequence, we do not believe that this signal will be observable in the near future.

### 3.4 Radio background produced by 21 cm emission

Perhaps the most promising observational signature comes from 21 cm emission of the relic H II region gas once the star has died, a prospect that was already investigated by Tokutani et al. (2009). An emission signal requires the spin temperature  $T_S$  of neutral hydrogen to be greater than the temperature of the CMB, with its relative brightness determined by  $T_S$  and the size of the relic H II region. The spin temperature is set by collisional coupling with neutral hydrogen atoms, protons and electrons, as well as radiative coupling to the CMB. Furthermore, it may be modified by the so-called Wouthuysen-Field effect, which describes the mixing of spin states due to the absorption and re-emission of Ly $\alpha$  photons (Wouthuysen 1952; Field 1959). The color temperature of the Ly $\alpha$  background is determined by the ratio of excitations to de-excitations, which approaches the kinetic gas temperature at high redshifts, where the optical depth to Ly $\alpha$  scattering is very large (Furlanetto et al. 2006). In this case, adopting the Rayleigh-Jeans approximation and assuming  $T_S \gg T_*$ , where  $T_* = h\nu_{21}/k_{\text{B}} = 68 \text{ mK}$  is the temperature associated with the 21 cm transition, the spin temperature may be written as (Madau et al. 1997)

$$T_S = \frac{T_{\gamma} + (y_c + y_{\alpha}) T}{1 + y_c + y_{\alpha}}, \quad (30)$$

where  $T_{\gamma}$  is the temperature of the CMB. The collisional coupling coefficient  $y_c$  is approximately given by

<sup>1</sup> <http://www.skatelescope.org>



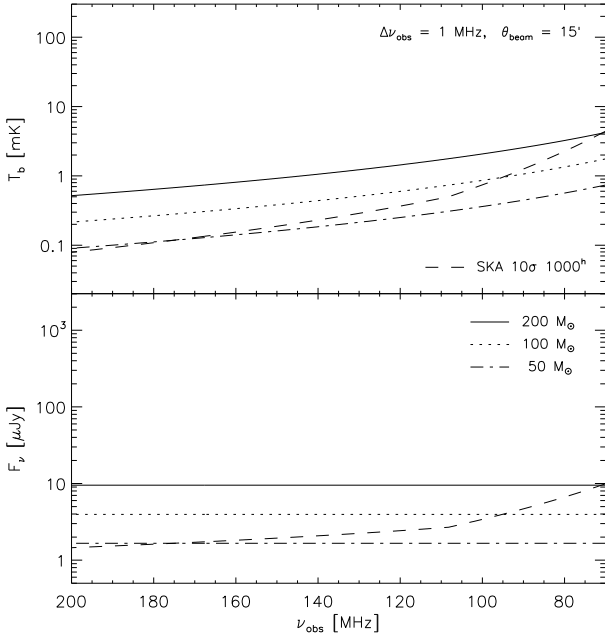


**Figure 5.** The brightness temperature and specific flux of the radio background produced by bremsstrahlung, shown as a function of observed frequency. We have chosen a beam size of  $15'$  to achieve the highest possible resolution and sensitivity at 100 MHz for the currently planned configuration of the SKA. The dot-dashed, dotted and solid lines correspond to an initial mass function consisting solely of 50, 100 and 200  $M_{\odot}$  Pop III stars, respectively. The dashed line shows the sensitivity of the SKA for a  $10\sigma$  detection, a bandwidth of 1 MHz, and an integration time of 1000 h. Although the free-free signal is in principle detectable by the SKA, we have here neglected biasing and radiative feedback, which act to reduce the signal. For this reason we do not believe that the free-free signal of the first H II regions in their active or relic states will be observable in the near future.

$$y_c = \frac{T_*}{A_{21}T} (n_{\text{HI}}\kappa_{\text{HI}} + n_e\kappa_e), \quad (31)$$

where  $A_{21} = 2.85 \times 10^{-15} \text{ s}^{-1}$  is the Einstein A-coefficient for the 21 cm transition, and  $\kappa_{\text{HI}}$  and  $\kappa_e$  are the effective single-atom rate coefficients for collisions with neutral hydrogen atoms and electrons, respectively. Good functional fits in the temperature range  $100 \text{ K} \lesssim T \lesssim 10^4 \text{ K}$  are given by

$$\kappa_{\text{HI}} = 10^{-11} T^{1/2} \text{ cm}^3 \text{ s}^{-1} \quad (32)$$

and

$$\kappa_e = 2 \times 10^{-10} T^{1/2} \text{ cm}^3 \text{ s}^{-1}, \quad (33)$$

which we have obtained from the rates quoted in Kuhlen et al. (2006). At  $z \lesssim 20$ , the electron fraction in the IGM remains above  $f_e = 0.1$  for most of the lifetime of the relic H II region. In this case, the collisional coupling coefficient is given by

$$y_c \simeq 0.015 \left(\frac{f_e}{0.5}\right) \left(\frac{T}{10^3 \text{ K}}\right)^{-1/2} \left(\frac{1+z}{10}\right)^3. \quad (34)$$

A derivation of the Ly $\alpha$  coupling coefficient  $y_{\alpha}$  requires radiative transfer of local as well as global Ly $\alpha$  radiation, which is beyond the scope of this work. We therefore consider two limiting cases: one in which we only consider collisional coupling, and the other in which a strong Ly $\alpha$  back-

ground drives the spin temperature towards the gas temperature (i.e.  $y_{\alpha} \gg 1$  or  $T_S = T$ ).

The differential brightness temperature with respect to the CMB may then be derived as follows. In the Rayleigh-Jeans limit and for  $T_S \gg T_*$ , the monochromatic radiative transfer equation for a ray passing through a cloud, evaluated in its comoving frame, may be written in terms of the brightness temperature  $T_b$ :

$$T_b = T_{\gamma} e^{-\tau} + \int_0^{\tau} T_S e^{-\tau'} d\tau', \quad (35)$$

where the optical depth at the 21 cm line is given by

$$d\tau = \frac{3c^2 A_{21} n_{\text{HI}}}{32\pi\nu_{21}^2} \phi(\nu_{21}) \frac{T_*}{T_S} ds. \quad (36)$$

Here,  $\phi(\nu_{21})$  is the normalised line profile at the resonance frequency  $\nu_{21}$  and  $ds$  is the distance traveled by the ray. In our case, the line profile is dominated by thermal broadening, with a Doppler width given by

$$\Delta\nu_{\text{D}} = \nu_{21} \sqrt{\frac{2k_{\text{B}}T}{\mu m_{\text{H}}c^2}}. \quad (37)$$

The amplitude of the line profile at the resonance frequency may be replaced by the Doppler width, i.e.  $\phi(\nu_{21}) = \Delta\nu_{\text{D}}^{-1}$ . With this definition, equation (35) yields the differential brightness temperature  $\delta T_b = T_b - T_{\gamma}$ , which becomes particularly simple for a constant spin temperature and the fact that the relic H II regions considered here are optically thin:

$$\delta T_b = (T_S - T_{\gamma}) \tau. \quad (38)$$

The observed differential brightness temperature is then simply given by  $\delta T_{b,\text{obs}} = \delta T_b / (1+z)$ .

In Fig. 6, we show the observed differential brightness temperature for a 100  $M_{\odot}$  star and the two limiting cases discussed above. Note that we have only taken into account ionised gas along the line of sight. For collisional coupling, the observed differential brightness temperature is of order a few 10 mK for  $\simeq 100$  Myr, while for perfect coupling the signal is elevated by an order of magnitude to a few 100 mK for well over  $\simeq 100$  Myr. In reality, the expected signal lies between these extremes and is a function of redshift, since collisional coupling becomes weaker as the background density drops, while Ly $\alpha$  coupling becomes stronger as the Ly $\alpha$  background rises. At  $z \lesssim 20$ , where the observationally accessible signal is produced, the Ly $\alpha$  background is likely strong enough for the latter to be more important (Furlanetto 2006; Pritchard & Furlanetto 2007).

Next, we determine the radio background produced by the integrated 21 cm emission of relic H II regions. The differential specific flux observed at the redshifted 21 cm line from a single relic H II region with differential brightness temperature  $\delta T_b$  is given by

$$\delta F_{\nu} = \frac{2k_{\text{B}}\nu_{21}^2}{c^2} (1+z)^{-3} \Delta\Omega \delta T_b, \quad (39)$$

where  $\Delta\Omega = A/D_{\text{A}}^2$  denotes the solid angle subtended by the relic H II region,  $A = \pi r_{\text{HII}}^2$  its area,  $r_{\text{HII}} = (3N_{\text{ion}}/4\pi n_{\text{H,b}})^{1/3}$  its radius, and  $D_{\text{A}}$  the angular diameter distance. The average differential specific flux  $\langle \delta F_{\nu} \rangle$  within a beam size  $\Delta\Omega_{\text{beam}}$  and bandwidth  $\Delta\nu_{\text{obs}}$  is then given by

$$\langle \delta F_{\nu} \rangle = \delta F N_{\text{ps}}(z) \frac{d^2V(z)}{dz d\Omega} \frac{\Delta z \Delta\Omega_{\text{beam}}}{\Delta\nu_{\text{obs}}}, \quad (40)$$

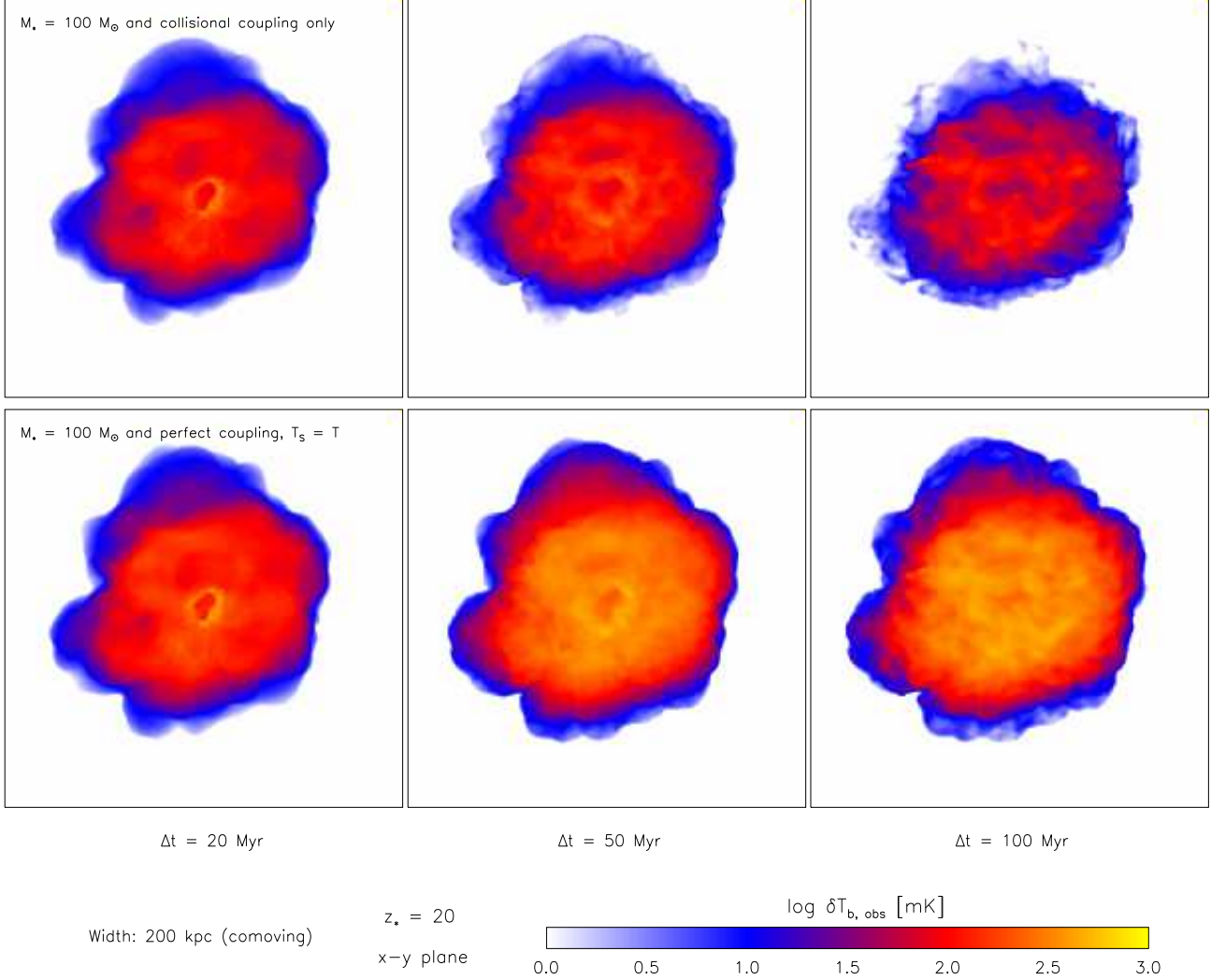


**Figure 6.** The observed differential brightness temperature of the relic H II region around a  $100 M_\odot$  Pop III star, shown 20, 50 and 100 Myr after the star has turned off. We delineate the range of possible values by showing the result for collisional coupling only (top row), as well as perfect coupling to the Ly $\alpha$  background, resulting in  $y_\alpha \gg 1$  or  $T_s = T$  (bottom row). In the first case, the observed differential brightness temperature is of order a few 10 mK for  $\simeq 100$  Myr, while in the second case the signal is of order a few 100 mK for well over  $\simeq 100$  Myr. We note that the latter is likely more relevant at  $z \lesssim 20$ , where the observationally accessible signal is produced (see Furlanetto 2006; Pritchard & Furlanetto 2007).

where  $\delta F = \delta F_\nu \Delta \nu_D / (1+z)$ ,  $N_{\text{ps}}(z)$  is the Press-Schechter mass function defined in equation (24),  $\Delta z = \Delta \nu_{\text{obs}} (1+z)^2 / \nu_{21}$ , and  $d^2V(z)/dz d\Omega$  is the comoving volume per unit redshift and solid angle:

$$\frac{d^2V(z)}{dz d\Omega} = \frac{c D_A^2 (1+z)^2}{H(z)}, \quad (41)$$

where  $H(z)$  is the Hubble expansion rate. With the definition of the brightness temperature, the average differential antenna temperature  $\langle \delta T_b \rangle$  is given by

$$\langle \delta T_b \rangle = \frac{\pi c}{\nu_{21}} \frac{(1+z)^2 N_{\text{ps}}(z)}{H(z)} \Delta \nu_D r_{\text{HII}}^2(z) \delta T_b(z). \quad (42)$$

Based on our argument above, we assume that the Ly $\alpha$  background is strong enough for perfect coupling at all redshifts. In this case, and for  $T \gg T_\gamma$ , the average differential antenna temperature becomes independent of electron fraction and temperature:

$$\langle \delta T_b \rangle = \frac{9c^3 A_{21} T_* N_{\text{ion}}}{128\pi \nu_{21}^3 H_0 \sqrt{\Omega_m}} (1+z)^{1/2} N_{\text{ps}}(z), \quad (43)$$

where we have set  $n_{\text{HI}} = n_{\text{H,b}}$  in equation (36). We note that the observed frequency is related to the redshift via  $\nu_{\text{obs}} = \nu_{21} / (1+z)$ . We have further assumed that the relic H II region produced by each star-forming minihalo persists until the Universe is reionised (i.e.  $z \simeq 6$ ), which is a good approximation for perfect coupling and  $T \gg T_\gamma$ . Equation (43) thus provides a robust upper limit for the collective 21 cm emission from the first relic H II regions.

In Fig. 7, we compare the average differential antenna temperature and specific flux for a beam size of  $\Delta \theta_{\text{beam}} = 15'$  to the sensitivity of the SKA, assuming a  $10\sigma$  detection, a bandwidth of  $\Delta \nu_{\text{obs}} = 1$  MHz, and an integration time of 1000 h. At all frequencies, the maximum 21 cm signal from the first relic H II regions is of order 10 mK, which is well detectable by the SKA. The effects of biasing and

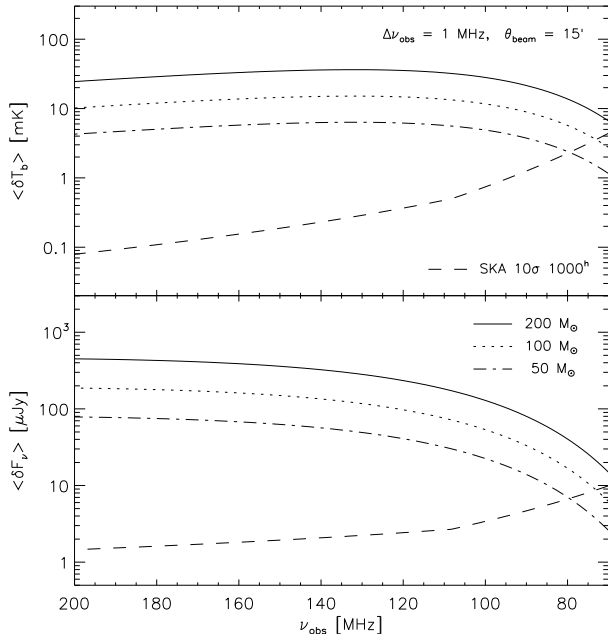


**Figure 7.** The average differential antenna temperature and specific flux of the radio background produced by 21 cm emission, shown as a function of observed frequency. We have chosen a beam size of  $15'$  to achieve the highest possible resolution and sensitivity at 100 MHz for the currently planned configuration of the SKA. The dot-dashed, dotted and solid lines correspond to an initial mass function consisting solely of 50, 100 and  $200 M_{\odot}$  Pop III stars, respectively. The dashed line shows the sensitivity of the SKA for a  $10\sigma$  detection, a bandwidth of 1 MHz, and an integration time of 1000 h. In all cases, the 21 cm signal is well above the detection threshold of the SKA. The effects of biasing and radiative feedback will reduce this signal, but probably not enough to fall below the sensitivity of the SKA. Compared to free-free emission, the 21 cm signal is typically an order of magnitude stronger, and offers the best prospect for indirectly probing the first stars.

radiative feedback will reduce this signal, but probably not enough to fall below the sensitivity of the SKA. Compared to free-free emission, the 21 cm signal is typically an order of magnitude stronger, and offers the best prospect for indirectly probing the first stars. Furthermore, the 21 cm signal is explicitly frequency-dependent, while this is not the case for bremsstrahlung, where a flat spectrum is produced (see equation 28). This dependency might allow for a better distinction from other sources of radio emission at these wavelengths.

#### 4 SUMMARY AND CONCLUSIONS

We have introduced a general-purpose radiative transfer scheme for cosmological SPH simulations that treats ionising and photodissociating radiation from massive Pop III stars in the early Universe. Based on this methodology, we have investigated the build-up of the first H II regions and relic H II regions around Pop III stars formed in minihaloes, and predicted their contribution to the extragalactic radio background via bremsstrahlung and 21 cm emission. Although recombination radiation from individual H II regions

in their active as well as relic states is too faint to be directly detectable even with *JWST*, their collective radio emission might be strong enough to be within reach of the planned SKA. In particular, we have found that the integrated free-free emission results in a maximum differential antenna temperature of  $\simeq 1$  mK, while the 21 cm emission is an order of magnitude stronger. Considering the effects of biasing and negative radiative feedback, which would act to reduce the predicted signal, the free-free signal is likely beyond the capability of the SKA, while the 21 cm signal will most likely be observable, providing an excellent opportunity for indirectly probing the first stars.

We note that an analysis of the angular fluctuation power spectrum will be essential to isolate the 21 cm signal from other backgrounds (Furlanetto & Oh 2006), although the frequency-dependence of the 21 cm signal might already prove useful. Among these are neutral minihaloes, which appear in emission due to their enhanced density and temperature (Iliev et al. 2002), or IGM gas heated by X-rays from supernovae (Oh 2001), X-ray binaries (Glover & Brand 2003), or the first quasars (Madau et al. 2004; Kuhlen et al. 2006). A strong absorption signal might originate from cold, neutral gas if the Ly $\alpha$  background effectively couples the spin temperature to the gas temperature (Pritchard & Furlanetto 2007). In addition, there is the signal produced by stars (primordial or already metal-enriched) formed in the first dwarf galaxies (e.g. Naoz & Barkana 2008). All of these compete with each other, and more work is required to understand their relative importance. One important task is to extend the simulations to larger cosmological volumes, to measure the aggregate signal from many sources in a more robust way.

Minihaloes may not have been the dominant formation sites for primordial stars, in terms of producing the bulk of the radiation that drove reionisation, or of being the source for the majority of the heavy elements present at high redshifts (Greif & Bromm 2006; Schleicher et al. 2008). Nevertheless, they are the ideal laboratory to test our current standard model of the first stars, by providing an exceedingly simple environment for the star formation process (Bromm et al. 2009). The next step in the hierarchical build-up of structure, more massive systems, such as the first galaxies, is already highly complex, due to the presence of metals, turbulent velocity fields, and possibly dynamically significant magnetic fields (Wise & Abel 2007, 2008; Greif et al. 2008; Schleicher et al. 2009). It is therefore crucial to empirically probe the minihalo environment, and the signature left in the radio background might provide us with one of the few avenues to accomplish this in the foreseeable future.

#### ACKNOWLEDGMENTS

The authors would like to thank the referee Naoki Yoshida for his valuable comments and suggestions that greatly improved this work. TG thanks Matthias Bartelmann and Simon Glover for many stimulating discussions. TG acknowledges financial support by the Heidelberg Graduate School of Fundamental Physics (HGSFP). The HGSFP is funded by the Excellence Initiative of the German government (grant number GSC 129/1). RSK acknowledge subsidies from the

*Deutsche Forschungsgemeinschaft* via the priority program SFB 439 “Galaxies in the Early Universe” as well as via grants KL1358/1, KL1358/4 and KL1358/5. In addition, RSK also acknowledges partial support from a Frontier grant of Heidelberg University funded by the German Excellence Initiative. VB acknowledges support from NSF grant AST-0708795 and NASA ATFP grant NNX08AL43G. The simulations presented here were carried out at the Texas Advanced Computing Center (TACC).

## REFERENCES

- Abel T., Bryan G. L., Norman M. L., 2002, *Sci*, 295, 93  
 Abel T., Wise J. H., Bryan G. L., 2007, *ApJ*, 659, L87  
 Alvarez M. A., Bromm V., Shapiro P. R., 2006, *ApJ*, 639, 621  
 Alvarez M. A., Shapiro P. R., Ahn K., Iliev I. T., 2006, *ApJ*, 644, L101  
 Barkana R., Loeb A., 2001, *Phys. Rep.*, 349, 125  
 Bromm V., Coppi P. S., Larson R. B., 2002, *ApJ*, 564, 23  
 Bromm V., Kudritzki R. P., Loeb A., 2001, *ApJ*, 552, 464  
 Bromm V., Larson R. B., 2004, *ARA&A*, 42, 79  
 Bromm V., Loeb A., 2003, *Nat*, 425, 812  
 Bromm V., Loeb A., 2004, *New Astron.*, 9, 353  
 Bromm V., Yoshida N., Hernquist L., 2003, *ApJ*, 596, L135  
 Bromm V., Yoshida N., Hernquist L., McKee C. F., 2009, *Nat*, 459, 49  
 Ciardi B., Ferrara A., 2005, *Space Sci. Rev.*, 116, 625  
 Clark P. C., Glover S. C. O., Klessen R. S., 2008, *ApJ*, 672, 757  
 Dijkstra M., Haiman Z., Rees M. J., Weinberg D. H., 2004, *ApJ*, 601, 666  
 Draine B. T., Bertoldi F., 1996, *ApJ*, 468, 269  
 Fan X., Carilli C. L., Keating B., 2006, *ARA&A*, 44, 415  
 Field G. B., 1959, *ApJ*, 129, 536  
 Furlanetto S. R., 2006, *MNRAS*, 371, 867  
 Furlanetto S. R., Oh S. P., 2006, *ApJ*, 652, 849  
 Furlanetto S. R., Oh S. P., Briggs F. H., 2006, *Phys. Rep.*, 433, 181  
 Gao L., White S. D. M., Jenkins A., Frenk C. S., Springel V., 2005, *MNRAS*, 363, 379  
 Gardner J. P., et al., 2006, *Space Sci. Rev.*, 123, 485  
 Glover S. C. O., Abel T., 2008, *MNRAS*, 388, 1627  
 Glover S. C. O., Brand P. W. J. L., 2001, *MNRAS*, 321, 385  
 Glover S. C. O., Brand P. W. J. L., 2003, *MNRAS*, 340, 210  
 Glover S. C. O., Jappsen A.-K., 2007, *ApJ*, 666, 1  
 Górski K. M., Hivon E., Banday A. J., Wandelt B. D., Hansen F. K., Reinecke M., Bartelmann M., 2005, *ApJ*, 622, 759  
 Greif T. H., Bromm V., 2006, *MNRAS*, 373, 128  
 Greif T. H., Johnson J. L., Bromm V., Klessen R. S., 2007, *ApJ*, 670, 1  
 Greif T. H., Johnson J. L., Klessen R. S., Bromm V., 2008, *MNRAS*, 387, 1021  
 Haiman Z., Abel T., Rees M. J., 2000, *ApJ*, 534, 11  
 Haiman Z., Loeb A., 1997, *ApJ*, 483, 21  
 Heger A., Woosley S. E., 2002, *ApJ*, 567, 532  
 Iliev I. T., Scannapieco E., Martel H., Shapiro P. R., 2003, *MNRAS*, 341, 81  
 Iliev I. T., Shapiro P. R., Ferrara A., Martel H., 2002, *ApJ*, 572, L123  
 Jappsen A.-K., Glover S. C. O., Klessen R. S., Mac Low M.-M., 2007, *ApJ*, 660, 1332  
 Jappsen A.-K., Klessen R. S., Glover S. C. O., MacLow M.-M., 2009, *ApJ*, 696, 1065  
 Johnson J. L., Greif T. H., Bromm V., 2007, *ApJ*, 665, 85  
 Johnson J. L., Greif T. H., Bromm V., 2008, *MNRAS*, 388, 26  
 Johnson J. L., Greif T. H., Bromm V., Klessen R. S., Ippolito J., 2009, *MNRAS*, in press (arXiv:0902.3263)  
 Kashlinsky A., Arendt R. G., Mather J., Moseley S. H., 2005, *Nat*, 438, 45  
 Kitayama T., Yoshida N., Susa H., Umemura M., 2004, *ApJ*, 613, 631  
 Kogut A., et al., 2006, *New Astron. Rev.*, 50, 925  
 Komatsu E., et al., 2009, *ApJS*, 180, 330  
 Kuhlen M., Madau P., Montgomery R., 2006, *ApJ*, 637, L1  
 Lazio J., 2008, in Minchin R., Momjian E., eds, *AIP Conf. Ser. Vol. 1035, The Evolution of Galaxies Through the Neutral Hydrogen Window*. Am. Inst. Phys., New York, p. 303  
 Loeb A., Rybicki G. B., 1999, *ApJ*, 524, 527  
 Madau P., Meiksin A., Rees M. J., 1997, *ApJ*, 475, 429  
 Madau P., Rees M. J., Volonteri M., Haardt F., Oh S. P., 2004, *ApJ*, 604, 484  
 Marigo P., Girardi L., Chiosi C., Wood P. R., 2001, *A&A*, 371, 152  
 McKee C. F., Tan J. C., 2008, *ApJ*, 681, 771  
 Mo H. J., White S. D. M., 1996, *MNRAS*, 282, 347  
 Naoz S., Barkana R., 2008, *MNRAS*, 385, L63  
 Oh S. P., 2001, *ApJ*, 553, 499  
 Oh S. P., Haiman Z., 2002, *ApJ*, 569, 558  
 Omukai K., Tsuribe T., Schneider R., Ferrara A., 2005, *ApJ*, 626, 627  
 Osterbrock D., Ferland G., 2006, *Astrophysics of Gaseous Nebulae and Active Galactic Nuclei*. University Science Books, Sausalito  
 Panagia N., 2005, in Corbelli E., Palla F., Zinnecker H., eds, *The Initial Mass Function 50 Years*. Springer, Berlin, p. 479  
 Press W. H., Schechter P., 1974, *ApJ*, 187, 425  
 Pritchard J. R., Furlanetto S. R., 2007, *MNRAS*, 376, 1680  
 Reed D. S., Bower R., Frenk C. S., Gao L., Jenkins A., Theuns T., White S. D. M., 2005, *MNRAS*, 363, 393  
 Rybicki G. B., Lightman A. P., 1979, *Radiative Processes in Astrophysics*. Wiley-Interscience, New York  
 Santos M. R., Bromm V., Kamionkowski M., 2002, *MNRAS*, 336, 1082  
 Scannapieco E., Madau P., Woosley S., Heger A., Ferrara A., 2005, *ApJ*, 633, 1031  
 Schaerer D., 2002, *A&A*, 382, 28  
 Schaerer D., 2003, *A&A*, 397, 527  
 Schleicher D. R. G., Banerjee R., Klessen R. S., 2008, *Phys. Rev. D*, 78, 083005  
 Schleicher D. R. G., Galli D., Glover S. C. O., Banerjee R., Palla F., Schneider R., Klessen R. S., 2009, submitted (arXiv:0904.3970)  
 Seiffert M., et al., 2009, submitted (arXiv:0901.0559)  
 Shu F. H., Lizano S., Galli D., Cantó J., Laughlin G., 2002, *ApJ*, 580, 969  
 Springel V., 2005, *MNRAS*, 364, 1105

- Tan J. C., McKee C. F., 2004, *ApJ*, 603, 383  
Tokutani M., Yoshida N., Oh S. P., Sugiyama N., 2009, *MNRAS*, 395, 777  
Tornatore L., Ferrara A., Schneider R., 2007, *MNRAS*, 382, 945  
Trenti M., Stiavelli M., 2009, *ApJ*, 694, 879  
Tumlinson J., Giroux M. L., Shull J. M., 2001, *ApJ*, 550, L1  
Vázquez G. A., Leitherer C., Schaerer D., Meynet G., Maeder A., 2007, *ApJ*, 663, 995  
Whalen D., Abel T., Norman M. L., 2004, *ApJ*, 610, 14  
Wise J. H., Abel T., 2007, *ApJ*, 665, 899  
Wise J. H., Abel T., 2008, *ApJ*, 685, 40  
Woosley S. E., Heger A., 2006, *ApJ*, 637, 914  
Wouthuysen S. A., 1952, *AJ*, 57, 31  
Yoon S.-C., Langer N., 2005, *A&A*, 443, 643  
Yoshida N., Abel T., Hernquist L., Sugiyama N., 2003, *ApJ*, 592, 645  
Yoshida N., Oh S. P., Kitayama T., Hernquist L., 2007, *ApJ*, 663, 687  
Yoshida N., Omukai K., Hernquist L., 2008, *Sci*, 321, 669